Turbine Blading Designed for High Heat Load Space Propulsion Applications

K. C. Civinskas*
and
R. J. Boyle†
NASA Lewis Research Center, Cleveland, Ohio 44135
and
H. V. McConnaughey†
NASA Marshall Space Flight Center, Alabama 35812

The operating conditions and the propellant transport properties used in Earth-to-orbit (ETO) applications affect the aerothermodynamic design of ETO turbomachinery in a number of ways. This paper discusses some aerodynamic and heat-transfer implications of the low molecular weight fluids and high Reynolds number operating conditions on future ETO turbomachinery. The objective of this work was to examine turbine blading concepts for increasing life and reliability by reducing thermal heat load. Using the current Space Shuttle main engine high-pressure fuel turbine as a baseline, aerothermodynamic comparisons were made for two alternate fuel turbine geometries. The first was a revised first-stage rotor blade designed to reduce peak heat transfer. This alternate design resulted in a 23% reduction in peak heat transfer. The second design concept was a single-stage rotor designed to yield the same power output as the baseline two-stage rotor. Since the rotor tip speed was held constant, the turbine work factor doubled. In this alternate design, the peak heat transfer remained the same as the baseline. Although the efficiency of the single-stage design was 3.1 points less than the baseline two-stage turbine, the design was aerothermodynamically feasible and may be structurally desirable.

Nomenclature

C_1 = slope of heat-transfer augmentation curve
C_p = specific heat
c = chord
D = leading-edge diameter
$\bar{e}$ = kinetic energy loss coefficient
h = heat-transfer coefficient
i = enthalpy
m = exponent in heat-transfer correlation
N_s = number of stages
Nu = Nusselt number based on diameter
Pr = Prandtl number
p = pressure
q = heat flux
R = gas constant
Re = Reynolds number based on blade leading-edge diameter
T = temperature
T_u = turbulence intensity
U = wheel speed
V = absolute velocity
v = specific volume
W = relative velocity
Z = compressibility factor
α = absolute flow angle
β = relative flow angle
γ = ratio of specific heats
$\Delta h'$ = output specific work
η = efficiency

Subscripts

cr = critical condition
g = fluid
in = inlet
m = mean
u = tangential
w = wall

Superscripts

$'$ = absolute total conditions
$''$ = relative total conditions
$*$ = definition used in analysis

Presented as Paper 88-3091 at the AIAA/ASME/SAE/ASEE 24th Joint Propulsion Conference, Boston, MA, July 11-13, 1988; received Aug. 22, 1988; revision received May 19, 1989.

*Aerospace Engineer, Propulsion Directorate, U. S. Army Aviation Research and Technology Activity—AVSCOM.
†Aerospace Engineer, Member AIAA.

Introduction

THE H_2 and O_2 propellants used in Earth-to-orbit (ETO) applications affect the aerothermodynamic design of propulsion systems in a number of ways. The design operating point in ETO applications is significantly different from conventional gas turbines. The low molecular weight fluid results in low-pressure ratios for relatively high stage specific work. The high system pressures result in high Reynolds numbers, which in turn result in high heat-transfer rates, even though the gas-to-wall temperature differences are relatively modest. This paper discusses some aerodynamic and heat-transfer implications of low molecular weight and high Reynolds numbers on future ETO turbomachinery configurations.

Even though ETO turbomachinery has characteristics different from conventional gas turbines, it also has a number of similarities to conventional air-breathing turbines. Table 1 gives the characteristics of the Space Shuttle main engine (SSME) high-pressure fuel turbine (HPFT) and the high-pressure oxidizer turbine (HPOT), as well as three representative air-breathing gas turbines. The air-breathing turbines shown

Table 1 Comparison of turbine design operating conditions

Description	NASA core turbine	E3	LART	SSME HPFT	SSME HPOT
	Actual conditions				
Number of turbine stages, N_S	1	1	1	2	2
Inlet total temperature, K	2200	1562	1644	1051	867
Inlet total pressure, kPA	3861	1324	802	38,094	38611
Mass flow rate, kg/s	49.40	27.91	9.60	74.80	29.67
Rotative speed, rpm	21,772	13,232	24,863	36,353	29,256
Specific work, kJ/kg	557.3	468.2	251.9	727.1	719.7
Pressure ratio, P'_{in}/P'_{out}	3.0	4.0	3.09	1.48	1.54
Blade speed-tip, m/s	579	568	549	538	412
Diameter-tip, cm	50.8	82.0	42.2	28.2	26.9
Power, kW	27,516	14,090	4020	54,360	21,350
Number of blades	64	54	50	63–59	78–73
Power per blade, kW	430	261	80.5	446	141
Mean radius, Re No. ($\times 10^{-6}$)	3.23	1.37	0.86	20.7	10.6
Work factor, $\Delta h'/U_m^2/N_S$	1.94	1.83	1.64	1.50	2.34
Reference	1	2	3	Engine balance	
	Equivalent conditions				
Inlet total temperature, K	288.2	288.2	288.2	288.2	288.2
Inlet total pressure, kPa	101.3	101.3	101.3	101.3	101.3
Mass flow, kg/s	3.71	5.11	2.98	1.09	0.404
Speed, rpm	8080	5779	10571	6792	5666
Specific work, kW/kg	76.8	89.3	75.8	25.4	27.0
Pressure ratio, P'_{in}/P'_{out}	3.44	4.45	3.37	1.48	1.55

in Table 1 are a NASA core turbine,[1] an energy efficient engine (E^3) turbine,[2] and a low aspect ratio turbine (LART).[3]

Except for high Reynolds numbers, the SSME turbines have many performance parameters in the same range as air-breathing turbines. In particular, it should be noted that the SSME fuel turbine has almost the same output power per stage as the NASA core turbine. The core turbine was designed for a high turbine inlet temperature, and in some ways the current ETO turbomachinery anticipates future gas turbine trends. Current ETO machinery has a combination of high heat-transfer coefficients and moderate gas-to-blade temperature differences, and future gas turbines will have higher gas-to-blade temperature differences as well as somewhat higher heat-transfer coefficients because of higher cycle pressures. If future gas turbines are operated at the same tip speed (same stress levels) as current machines, they will have higher work factors using current design practices. Although this paper specifically addresses design alternatives for ETO propulsion, it is felt that these same concepts may also be applicable to future high-temperature air-breathing turbines.

This paper evaluates the impact of ETO fluids by considering two alternate designs for ETO turbomachinery. The current two-stage SSME fuel turbine is used as a baseline for comparison purposes. The first alternate is a redesign of the first-stage rotor in order to reduce peak heat transfer. The second alternate is a single-stage design for the same work output as the baseline two-stage turbine. Both rotor designs had the same rotor tip speed as the baseline case, and the geometry was chosen to prevent flow separation.

Method of Analysis

Aerodynamic and heat-transfer analyses were done for each design. The aerodynamic predictions used a quasi-three-dimensional inviscid flow analysis. The flow analysis was done using the MERIDL code developed by Katsanis and McNally[4] coupled to the PANEL code of McFarland.[5] The results of the flow analysis were coupled to boundary-layer analyses. The predicted aerodynamic efficiency was calculated using the procedure given by Boyle et al.[6] The heat-transfer analysis used the STAN5 finite-difference boundary-layer code of Crawford and Kays.[7] The aerodynamic efficiency procedure utilized the integral boundary-layer code BLAYER, developed by McNally.[8] The PANEL code was used for the analysis of the flow along the blade surface because of its ability to obtain an accurate definition of the flow in the blade leading-edge region. The PANEL code was used to determine freestream velocity distributions for both heat-transfer analysis and isothermal boundary-layer analyses for the blade rows to ensure that the flow did not separate. The verification of attached flow was done by specifying isothermal conditions because this was more conservative than the cooled-wall assumption in determining possible flow separation. In the evaluation of aerodynamic efficiencies, only aerodynamic losses were considered. Therefore, the predicted efficiency was greater than the actual machine efficiency. Heat-transfer analysis was done using the STAN5 boundary-layer code, except in the leading-edge region. In this region, an experimental correlation was used. Figure 1 shows an outline of the analytic procedure.

It is possible to perform an aerodynamic analysis of ETO turbomachinery by using an air-equivalent analysis. However, the heat-transfer analysis requires that, in addition to the Mach and Reynolds numbers, there must be a match of Prandtl and Eckert numbers. The additional constraints prohibit a straightforward air-equivalent analysis for ETO turbomachinery, and the aerothermodynamic analyses were done by using actual fluid properties. Both boundary-layer analyses (BLAYER and STAN5) were modified to utilize mixture properties of the ETO fluids, steam, and H_2. These properties were obtained from the WASP code of Hendricks et al.,[9] and the GASP code of Hendricks et al.[10] The use of mixture properties resulted in a changing of the base enthalpy with mixture ratio. To facilitate the use of STAN5 with different mixture ratios, the program was changed to allow the specification of temperatures in place of enthalpies for the initial and boundary conditions.

The aerodynamic analysis of gas turbines is generally done by assuming an ideal gas. At the SSME turbomachinery temperatures and pressures, there are significant compressibility effects. Constant compressibility can be accounted for in a

straightforward manner, but variable compressibility may affect the prediction of turbine work. Appendix A contains a discussion of the appropriate correction for variable compressibility in the determination of output work. It is shown that for the cases investigated the correction is less than 2%, but may not be as small in other circumstances.

The heat-transfer analyses were performed with a constant wall-to-gas temperature ratio of 0.7. This was done to determine heat-transfer coefficients that were not strongly affected by the wall-to-gas temperature difference. The STAN5 analysis calculates the heat flux from the temperature gradient of the fluid adjacent to the wall. The local heat-transfer coefficient is calculated from the heat flux and a specified temperature difference. The temperature difference is normally expressed as the difference between the wall and recovery temperatures. For Pr other than 1, the recovery temperature is a function of the local freestream velocity. The local recovery factor equals $\sqrt[3]{Pr}$, and the ETO propellants have mixture Prandtl numbers between 0.5 and 0.6. The heat-transfer coefficient can be expressed in terms of the freestream velocity ratio as

$$h = \frac{\dfrac{q}{T''_q}}{1 - \left(\dfrac{\gamma-1}{\gamma+1}\right)\left(\dfrac{W}{W_{cr}}\right)^2\left(1 - \sqrt[3]{Pr}\right) - \dfrac{T_w}{T''_g}} \tag{1}$$

By choosing a wall-to-gas temperature ratio of 0.7, the local heat-transfer coefficient is nearly independent of the local recovery temperature. Having heat-transfer coefficients dependent on fluid property variations, but not on the wall-to-gas temperature ratio, facilitates the calculation of heat-transfer coefficients during startup and shutdown conditions when the flow conditions are not precisely known. The equation for h shows it to be affected by the freestream velocity ratio. For comparison purposes, it is better to use an effective heat-transfer coefficient that compares heat load to the blade on a consistent basis, and is unaffected by freestream velocity differences. Defining h as $q/(T''_q - T_w)$ does just this, and thus is the definition used herein.

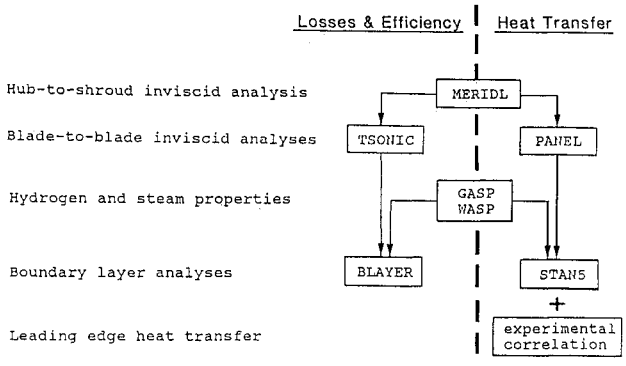

Fig. 1 Outline of procedure used in analysis.

The heat transfer in the leading-edge region is based on experimental data, and Fig. 2 shows the correlation used. In this figure, the ratio $Nu/\sqrt{Re}$ is shown as a function of $T_u\sqrt{Re}$. Also shown in this figure are the abscissa values for the baseline and alternate designs. These values are for the predicted flow conditions at the hub and a T_u of 0.10. This value of 10% was calculated from the baseline stator geometry and the gap between the stator and rotor. The value of T_u is subject to a high level of uncertainty, and a different value would affect the absolute level of the heat transfer. Fortunately, relative comparisons would be much less affected. The experimental data from a number of sources are shown. There are very little data near the high abscissa values of the baseline and alternate designs. There are only the two experimental data points of Žukauskas and Žiugžda[11] for abscissa vales greater than 57, whereas the three cases analyzed have values between 72 and 217. The correlation of Lowery and Vachon[12] shows a leveling off of the heat-transfer augmentation, whereas a straight line was used in the design study. The data of O'Brien and Van Fossen[13] indicate a linear relationship for the heat-transfer augmentation. The straight-line correlation used is conservative because the benefit of a larger leading edge is reduced due to higher augmentation. All of the data for Fig. 2 are for air and show no Prandtl number effect. The Nusselt number is a function of both the Reynolds and Prandtl numbers. To account for the different Prandtl number of the ETO fluid mixture, the Nusselt number was multiplied by the ratio $\sqrt[3]{Pr_{fluid}/Pr_{air}}$.

The straight-line correlation used in the analysis has an upper limit of applicability, beyond which the augmentation increases at a slower rate. The change in heat transfer with respect to Re would not exceed that for turbulent flow. In turbulent flow, $Nu \propto Re^m$.

Then

$$\frac{dNu}{Nu} = m\frac{dRe}{Re} \tag{2}$$

For the straight-line correlation shown in Fig. 2,

$$\frac{Nu}{\sqrt{Re}} = 1 + C_1 T_u \sqrt{Re} \tag{3}$$

The Reynolds number at which the Nusselt number in this augmented heat-transfer equation increases as fast as for turbulent flow is given as

$$Re_{max} = \left[\frac{m - 0.5}{C_1 T_u (1 - m)}\right]^2 \tag{4}$$

The exponent in the heat-transfer correlation m is 0.8 for turbulent flow. The slope of the augmented heat transfer C_1 is 0.008. When $T_u = 0.1$, $Re_{max} = 3.52 \times 10^6$.

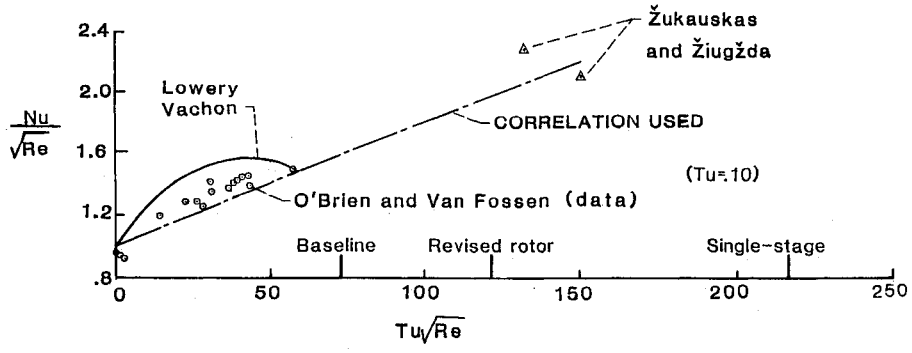

Fig. 2 Heat-transfer correlation for rotor leading edge.

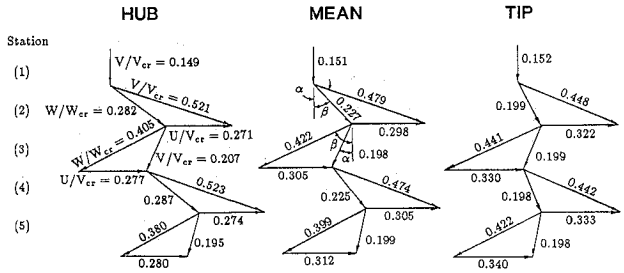

$\alpha_2 =$	71.5	70.0	67.2
$\beta_2 =$	53.4	42.8	27.7
$\alpha_3 =$	−24.1	−24.1	−22.6
$\beta_3 =$	−62.4	−65.0	−65.6
$\alpha_4 =$	69.8	68.1	65.6
$\beta_4 =$	50.3	37.3	20.9
$\alpha_5 =$	−15.8	−11.8	−11.5
$\beta_5 =$	−60.6	−61.1	−62.9

Fig. 3 Velocity diagram for baseline and revised rotor.

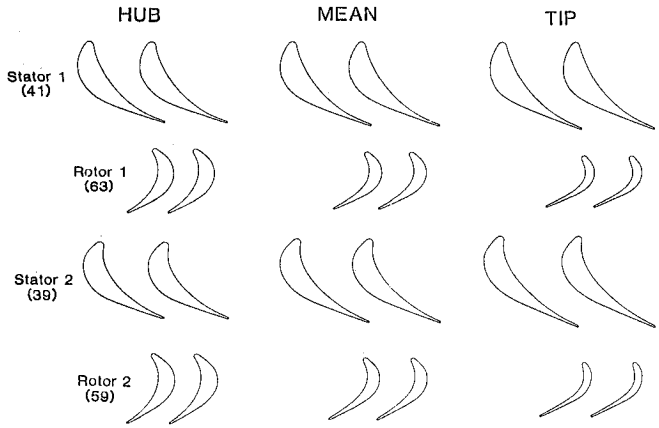

Fig. 4 Baseline blade geometry.

Baseline Case

The SSME two-stage high-pressure fuel turbine was used as the baseline for comparison purposes. Figure 3 shows the velocity diagrams for the four blade rows. Figure 4 shows the relationship of the four blade rows at the hub, mean, and tip sections. Figure 5 gives the meridional view of the baseline and revised flowpath. Also shown in this figure for later reference is the meridional view for the single-stage design. The calculated inviscid blade surface velocities for all four baseline blade rows are shown in Fig. 6.

The predicted heat-transfer distribution along the blade surface at the hub, mean, and tip sections for the first-stage rotor are shown in Fig. 7. For ease of comparison, the heat-transfer predictions for the revised rotor are also shown in this figure. The baseline case is an uncooled turbine in which almost all of the heat transfer to the blade occurs near the hub. Nevertheless, heat-transfer predictions are shown for both sections because future applications may be for a cooled turbine. Under this condition, the spanwise variation of heat transfer becomes more significant. The heat-transfer coefficients are highest in the leading-edge region. Along the suction surface, the heat transfer first decreases substantially and then changes more slowly. This behavior is the combined result of the surface velocities shown in Fig. 6 and the distance along the blade. If the velocity was constant, the heat transfer would decrease. However, the velocities increase with distance along the suction surface of the blade, and the overall result is relatively constant heat transfer. Along the pressure surface, the heat transfer decreases to a minimum, and then approaches the same value as the suction surface near the trailing edge. This is the result of the lower velocities along this surface. Transition is not a factor in these heat-transfer distributions. The Reynolds numbers are great enough that transition

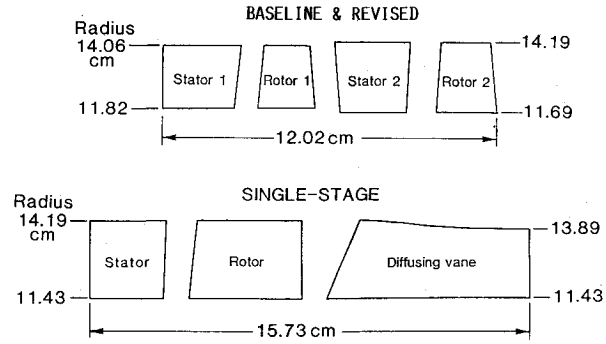

Fig. 5 Meridional flowpath geometry.

is complete within the leading-edge region, and it is here the experimental correlation is used.

Revised Rotor

The blade geometry for the revised first-stage rotor is shown in Fig. 8. This rotor was designed with a much larger leading-edge diameter than the baseline case in order to reduce the peak heat transfer. The revised rotor is much thicker than the baseline one, so that a hollow blade would be needed to satisfy structural constraints. Appendix B gives the geometric coordinates for the revised rotor as well as for the three blade rows of the single-stage design. It should be noted that the flow conditions into and out of the revised rotor are the same as for the baseline case. The velocity distributions are shown in Fig. 9 for the revised rotor at the three sections. Figure 7 gives the corresponding heat-transfer distributions. The revised rotor has lower peak heat transfer. In the critical hub region it is reduced by 23%. From Fig. 2, it can be seen that the augmentation in leading-edge heat transfer for the revised rotor is 1.93. If the correlation of Lowery and Vachon was valid at very high Reynolds numbers, both the baseline and revised rotor would have augmentation factors of 1.6. In this case, the leading-edge heat transfer would be reduced by 35% for the revised rotor case.

There are fewer blades (43) for the revised rotor than for the baseline rotor (63). This was done to keep the maximum surface heat transfer lower than the leading-edge heat transfer. The large leading edge results in increased blockage, which in turn results in increased surface velocities downstream of the leading edge. By reducing the blade count, the increase in surface velocity can be more easily controlled so that the heat transfer does not exceed the leading-edge value. Because the blade aerodynamic loading increases as the blade count is reduced, higher suction surface velocities occur in the tip region. Consequently, there is little overall reduction in the suction surface heat transfer in the tip region for the revised rotor. It was felt that reduced hub heat transfer in the high-stress region was more beneficial than a smaller uniform reduction over the entire span. The pressure surface heat-transfer distributions are essentially driven by the surface velocities. The appropriate blade shape and blade count are largely determined by the leading-edge heat transfer. If the augmentation due to turbulence is less, the blade shape and count should be modified to obtain the maximum reduction in heat transfer at the appropriate spanwise location.

The overall heat load to the blades is important when actively cooled blades are used. Figure 7 shows that the difference in the average heat-transfer coefficient for the entire blade between the baseline and revised rotor cases is not large. However, the surface area of each of the revised blades is only 10% greater than the surface area of each of the baseline blades, and the number of blades is reduced by over 30%. Consequently, the overall heat load would be reduced over 20% for the revised rotor, even if the average heat-transfer coefficients were the same.

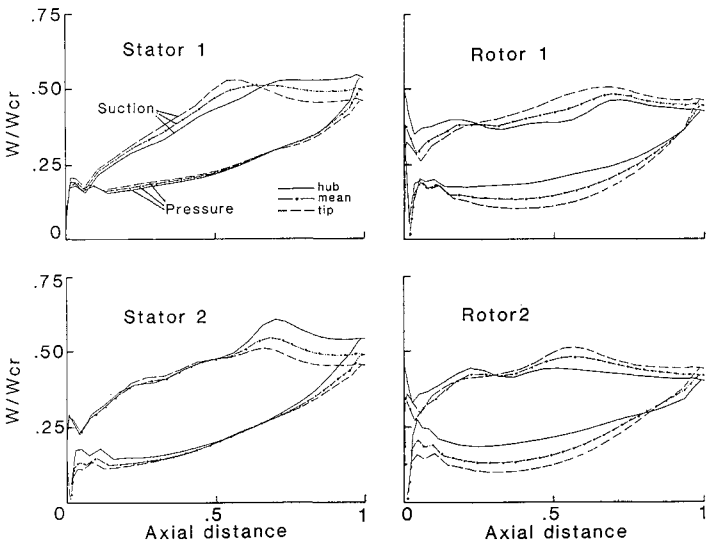

Fig. 6 Blade surface loadings for baseline.

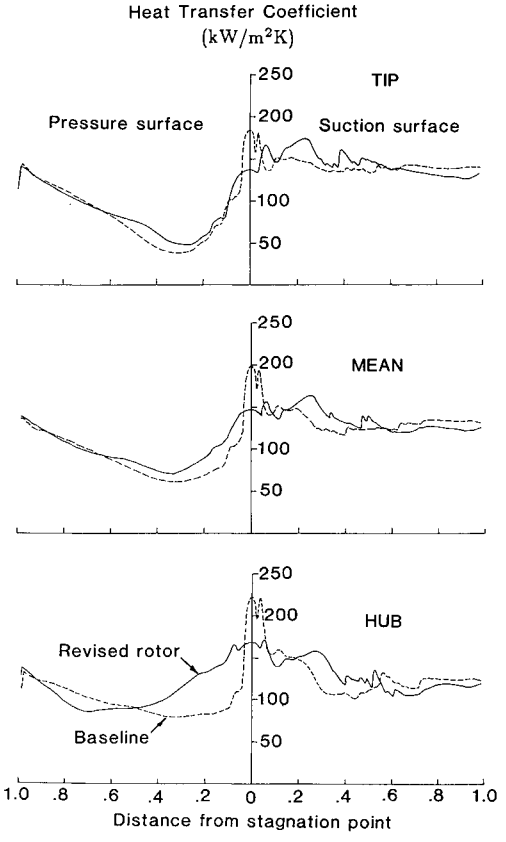

Fig. 7 Heat-transfer coefficients for baseline and revised rotor.

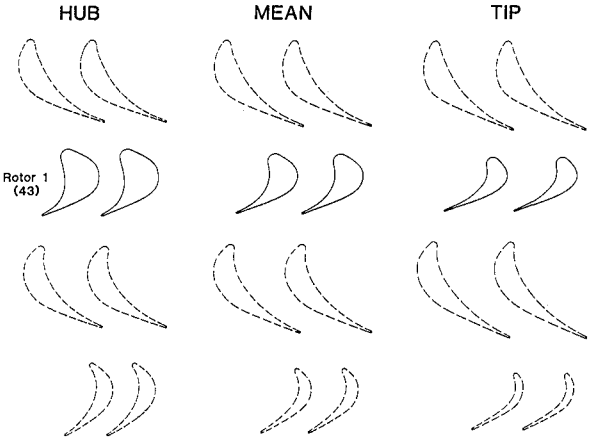

Fig. 8 Revised rotor blade geometry.

Table 2 gives a comparison of the loss breakdown for the three designs. For the revised first-stage rotor of the two-stage turbine, the analysis indicates changes in loss only for the first-stage rotor. As shown in part (a) of Table 2, the overall total-to-total efficiency for the revised rotor is 90.7% compared with an efficiency of 90.9% for the baseline case. This small decrement of 0.2 percentage points in efficiency is almost entirely due to increased profile loss for the revised rotor. The velocity distributions show that there is significantly more diffusion for the revised rotor. Even though the flow did not separate, the average momentum thickness for the revised rotor was nearly twice that of the baseline case. The high Reynolds numbers result in relatively thin boundary layers, so that even though the momentum thickness doubled, the loss in efficiency was only 0.2 points.

Figure 2 shows that the revised rotor has a value of $T_u\sqrt{Re}$ at the hub equal to 121 and is in excess of most of the experimental data base for the leading-edge heat-transfer augmentation. If the same approach of revising the blade shape to reduce peak heat transfer was applied to air-breathing gas turbines, it is likely that the revised blade shape would also be in the region of little data. For example, the air-breathing core turbine of Ref. 1 had a hub leading-edge diameter to chord ratio D/c of 0.11, and the ETO baseline case has a value of D/c of 0.074. If large leading-edge blades were used to reduce peak heat transfer in air-breathing turbines, it is likely that the leading-edge heat-transfer augmentation would be outside most of the current experimental data. The air-breathing core turbine would have an abscissa value of 31 if it were plotted in Fig. 2. The ratio of Reynolds numbers can be used to estimate the abscissa values for the air-breathing core turbine when the leading-edge diameter is increased to reduce the heat load. Use of the same ratios for the air-breathing core turbine as were used for the revised ETO blading results in abscissa values in Fig. 2 of 52 and 93. The latter value of 93 is in excess of most of the experimental data and even for the ETO baseline case.

In addition to modifying the shape of the rotor blade, there are other approaches that can be used to reduce heat transfer. The velocity diagram can be modified. Reducing the first-stage stator exit swirl would reduce the rotor inlet relative velocity. This would reduce the Reynolds number, and if used in conjunction with a revised blade geometry, could result in

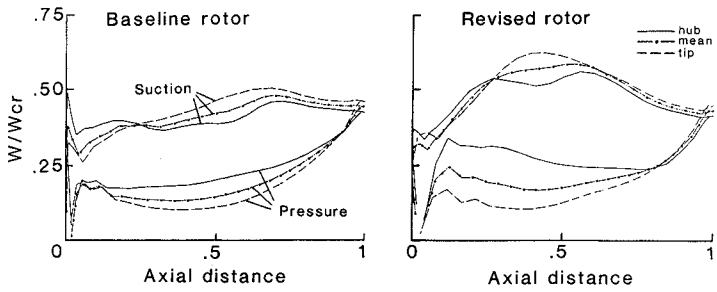

Fig. 9 Comparison of blade surface loadings for baseline and revised rotor.

Table 2 Turbine performance comparisons

	Baseline	Revised rotor	Single stage
Overall characteristics			
Output, kW	59022	58888	58388
Flow rate, kg/s	71.7	71.7	71.7
Pressure ratio			
Total-to-total	1.487	1.487	1.502
Total-to-static	1.521	1.521	1.542
Aerodynamic efficiency			
Total-to-total	0.909	0.907	0.878
Total-to-static	0.863	0.861	0.828
Individual blade row characteristics			
First-stage stator			
$\bar{e}$ profile	0.0212	0.0212	0.0252
Endwall	0.0103	0.0103	0.0094
Secondary	0.0076	0.0076	0.0041
Efficiency change $\Delta\eta$	0.028	0.028	0.035
First-stage rotor			
$\bar{e}$ profile	0.0267	0.0311	0.0449
Endwall	0.0030	0.0037	0.0068
Secondary	0.0152	0.0165	0.0283
Clearance	0.0799	0.0801	0.0469
Efficiency change $\Delta\eta$	0.072	0.075	0.073
Stage efficiency η	0.900	0.897	0.892
Stage pressure ratio	1.230	1.230	1.492
Second-stage stator			
$\bar{e}$ profile	0.0207	0.0207	
Endwall	0.0099	0.0099	
Secondary	0.0051	0.0051	
Efficiency change $\Delta\eta$	0.026	0.026	
Second-stage rotor			
$\bar{e}$ profile	0.0283	0.0283	
Endwall	0.0034	0.0034	
Secondary	0.0146	0.0146	
Clearance	0.0624	0.0624	
Efficiency change $\Delta\eta$	0.060	0.060	
Stage efficiency η	0.914	0.914	
Stage pressure ratio	1.209	1.209	
Exit guide vane			
$\bar{e}$ profile			0.0276
Endwall			0.0826
Secondary			0.0672
Efficiency change $\Delta\eta$			0.014
Guide vane pressure ratio			1.007

no increase in the heat-transfer augmentation factor. However, the lowered inlet swirl would require higher rotor exit flow angles in order to maintain the same amount of work. This in turn would require a redesign of the second-stage stator. Rather than pursue this approach, the alternate single-stage design was investigated, because it would address the same problems.

Single-Stage Design

The single-stage design resulted in approximately the same specific work as the baseline two-stage design. Consequently, the single-stage rotor has twice the change in tangential velocity as the baseline first-stage rotor. The stator design was changed from the baseline case so as to provide increased rotor inlet swirl. This gave a resulting work factor of 3.0. After the work was extracted, there was a large amount of rotor exit swirl. The single-stage turbine incorporates an exit diffusing vane to reduce the swirl to the same extent as in the baseline case. The designs of the stator, rotor, and diffusing vane will be discussed. Figure 10 gives velocity diagrams for the three-blade-row single-stage turbine. Figure 5 shows the meridional view of the flowpath. The radius at the hub was decreased to increase the span height over the baseline case. This was done primarily to minimize the inlet Mach numbers to the rotor and diffuser. The tip radius was decreased in the rearward part of the diffusing vane to give a similar annulus area for both the single-stage and baseline cases. Figure 11 shows the blade shapes for each of the three blade rows at sections corresponding to the hub, mean, and tip. The shape of the single-stage rotor was dictated by the desire to avoid separated flow in combination with a high hub incoming relative velocity. Consequently, the blade was very thick, and, just as with the revised rotor, it needed to be hollow to satisfy structural constraints. The exit guide vane had a complex shape, and Fig. 12 shows a three-dimensional view of the vane. The performance loss breakdown for the single-stage turbine is also given in Table 2. The single-stage design has a total-to-total efficiency of 3.1 points less than the baseline case. Because the exit conditions out of the single-stage exit guide vane were not exactly the same as for the baseline case, the change in total-to-static efficiency was greater than the change in total-to-total efficiency. The increase in total-to-static efficiency was 3.5 points.

Stator Design

The stator was designed to achieve the necessary swirl with low losses. The overall stator kinetic energy loss coefficient $\bar{e}$ was calculated as 0.039, with a profile component of 0.025. The stator is characterized by a large leading edge compared with the baseline case. Although an increased leading-edge diameter is desirable from a heat-transfer standpoint, the actual blade shape was determined primarily by aerodynamic considerations. The blade shape was determined primarily by the low solidity (chosen to give low profile loss) and a pressure-surface pressure distribution designed to avoid separation. Figure 13a shows the calculated inviscid surface velocities at the hub, mean, and tip sections. Schwab[14] gave aerodynamic data for similar highly turned stators having low profile loss.

Rotor Design

The high work factor resulted in a relatively high solidity rotor. The very high blockage shown in Fig. 11 for the hub is the result of the three-dimensional nature of the flow. At the hub, the streamsheet thicknesses at the rotor inlet and exit were nearly the same. However, in the middle of the passage, when the flow was axial, the streamsheet thickness was twice the value at the inlet. The high blockage was then used to minimize diffusion. In addition to acceptable aerodynamics, the rotor shape was maintained so that the peak heat transfer

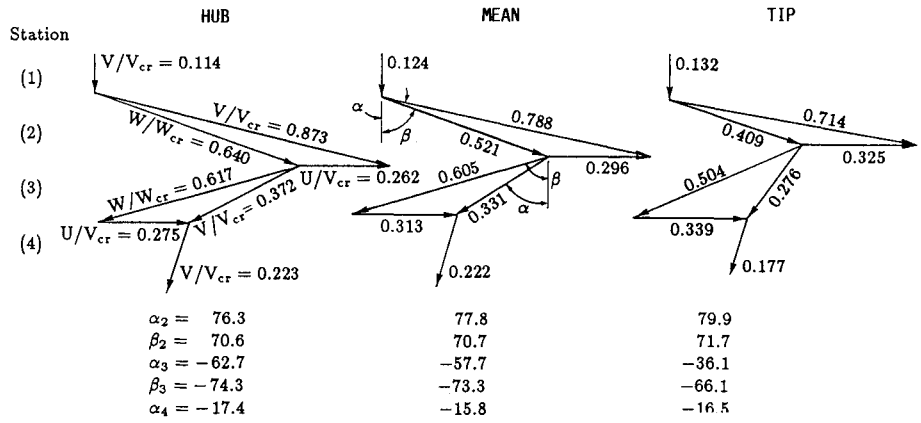

Fig. 10 Velocity diagram for single stage.

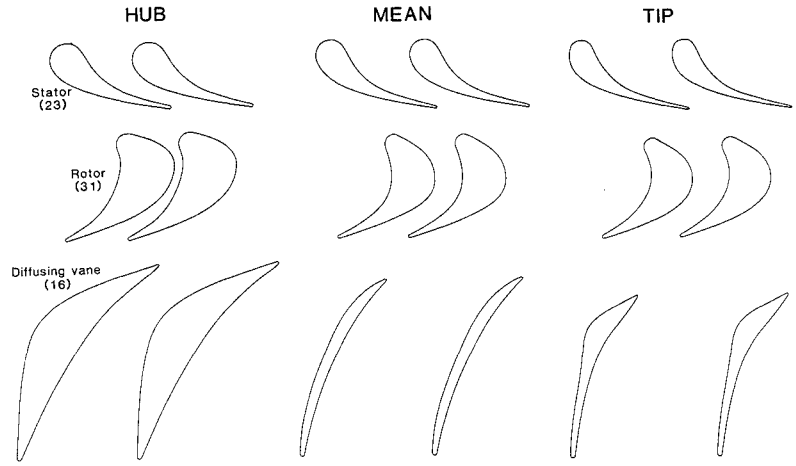

Fig. 11 Single-stage blade geometry.

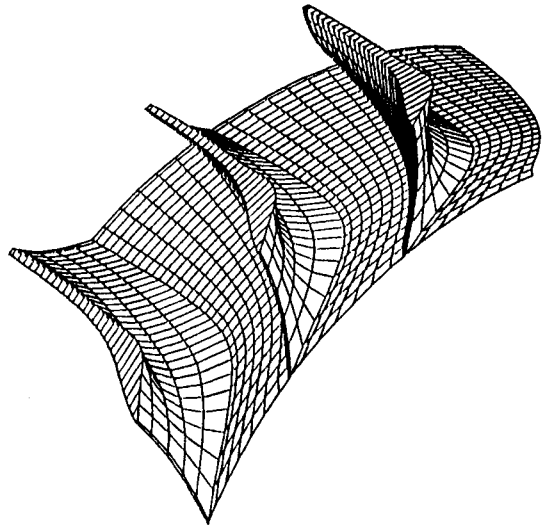

Fig. 12 Three-dimensional view of diffusing vane.

(at the leading edge) was about the same as in the baseline case.

The heat load to the rotor was reduced because of the lower rotor inlet T'' compared with the baseline case. The ratio T''/T'_{in} was 3% less for the single-stage design, and for a baseline T_w/T''_g of 0.7 this would be a 9% reduction in heat load. The calculated inviscid surface velocities are shown in Fig. 13b, and the heat-transfer coefficients are shown in Fig. 14. The effect of a less conservative assumption for the leading-edge heat transfer would result in the single-stage rotor having peak transfer significantly less than the baseline case. If the leading-edge heat-transfer augmentation were only 1.6 instead of 2.7, the leading-edge heat transfer would be 40% less than the baseline case. Figure 14 shows that the blade surface heat transfer is almost 30% less than the leading-edge value. Lower leading-edge heat transfer would not simply shift the peak heat transfer further back on the blade but would substantially reduce the peak heat transfer.

All of the revised blading was designed to avoid separated flow. Therefore, no incidence penalty was assigned in the loss calculation. There exists the potential for large incidence loss for the single-stage rotor due to the large W_{in} to the rotor. For the baseline rotor, the value at midspan of $W_{in}^2/U\Delta V_u$ is 0.28, whereas for the single-stage rotor it is 0.83. If the sensitivity of loss to off-optimum incidence were the same for both the baseline and single-stage designs, the decrement in efficiency would be three times greater for the single-stage design. However, since the blade shapes are different, it is not known what the off-design point incidence loss would be when the flow separates. The effect of incidence on the off-design point performance for blades of this type needs to be determined in order to be able to predict a performance map. Fortunately, the ETO turbomachinery operates very close to a single operating point. Future ETO turbines may require the same operating flexibility as air-breathing turbines. The aerodynamic efficiency of rotors designed to minimize leading-edge heat transfer needs to be determined over a range of incidence values.

In the design of the rotor, it is important to be able to predict accurately the exit flow conditions. This is especially true in the single-stage design. If the flow along the diffusing vane were to separate, it would be unlikely to reattach, and the efficiency of the single-stage design would be significantly

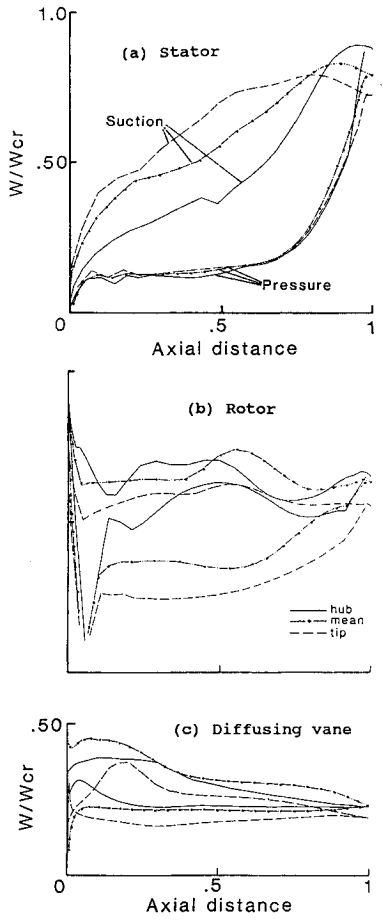

Fig. 13 Blade surface loadings for single stage.

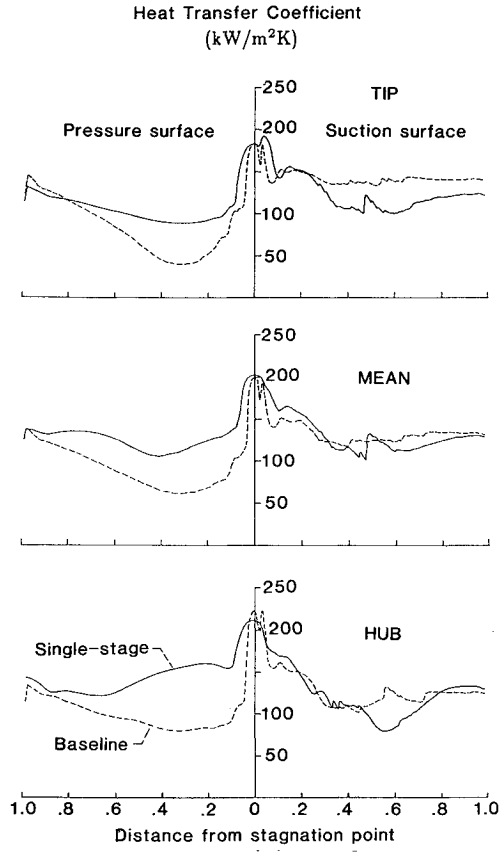

Fig. 14 Heat-transfer coefficients for single-stage rotor.

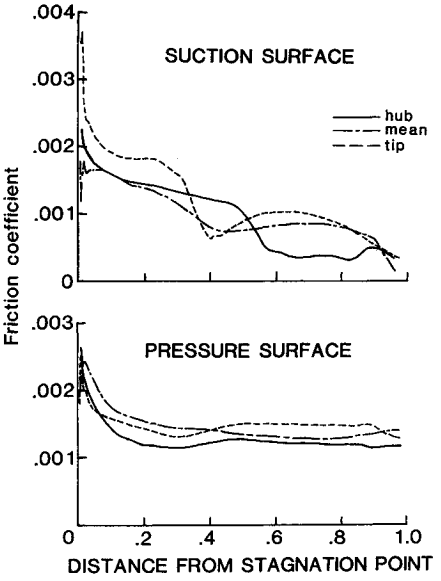

Fig. 15 Friction coefficient for diffusing vane.

lowered. It was found that the rotor exit flow angles were sensitive to the spanwise distribution of loss. The loss distribution was based on experimental results. Ewen et al.[15] showed that the effect of clearance generally was noticeable from the tip to midspan. The analytic model used in the current study assumed that all losses except for clearance loss were distributed uniformly in the spanwise direction. The clearance loss was distributed in a triangular fashion from midspan to the tip. Consequently, the clearance loss at the tip was nearly four times what it would have been if a uniform clearance loss distribution had been used. Variations in the assumed loss distribution only affect flow-angle predictions. The effect on blade row loss prediction is very small.

Exit Guide Vane

The primary consideration in the design of the exit guide vane was the avoidance of separation. Figure 13c shows the aerodynamic loadings for the diffuser vanes, and Fig. 15 shows the calculated friction factors for the suction and pressure surfaces at the hub, mean, and tip sections. The results presented by Sanz[16] were used as a guide for the initial blade configuration. The results given in this reference were for a two-dimensional blade-to-blade analysis. As can be seen in Fig. 12, the exit guide vane has a highly three-dimensional shape. The initial vane profiles were modified to account for changes in the stream-tube thicknesses as the swirl was removed. The thin leading edge of the exit guide vane results from tailoring the blade shape to avoid separation near the leading edge. Heat transfer was not a consideration in the design of the exit guide vane because the work extraction in the rotor significantly reduced the total temperature. The total temperature into the exit guide vane is 91% of the stator inlet total temperature, and is nearly the same as the total temperature at the exit of the second stage of the baseline case.

Conclusions

The results of this analysis show that significant reductions in peak heat transfer can be achieved for future ETO turbomachinery. Since the maximum heat transfer occurs in the leading-edge region, the magnitude of the reduction is strongly dependent on accurate knowledge of the leading-edge heat transfer. Both the blade shape and blade count are determined by the desired heat-transfer distributions. The analysis shows that blades can be designed for significantly lowered heat transfer without compromising aerodynamic efficiency. On the basis of a conservative assumption of leading-edge heat

transfer, the peak heat transfer in the hub region can be reduced by 23%. If the heat-transfer augmentation is constant at ETO turbomachinery Reynolds numbers, the peak heat transfer can be reduced as much as 35%.

An aerothermodynamic analysis of a single-stage design with the same output power and tip speed as the baseline two-stage design shows that the approach has merit. A doubling of the work factor over the baseline case appears feasible. The analysis shows no increase in peak heat-transfer rates over the baseline case. However, there is some penalty in overall turbine efficiency. The predicted total-to-total efficiency is 3.1 points less, and the total-to-static efficiency is 3.5 points less. The results show that turbine-blade profiles can be tailored to achieve significant reductions in heat transfer while still maintaining acceptable aerodynamic performance. In each specific application, the appropriate configuration would involve structural as well as aerothermodynamic considerations.

Appendix A: Calculation of Output Work for Nonideal Gas

This appendix contains a comparison of the work expression used in the analysis to the work of a nonideal fluid. The equation of state is

$$pv = ZRT \tag{A1}$$

The analysis uses a differential work expression given by

$$di^* = \frac{ZR\gamma}{(\gamma-1)}\,dT \tag{A2}$$

For the real fluid,

$$di = C_p dT - \left[T\left(\frac{\partial v}{\partial T}\right)_p - v\right] dp \tag{A3}$$

where C_p is given by

$$C_p = -\frac{\gamma}{(\gamma-1)}\,T\left(\frac{\partial v}{\partial T}\right)_T\left(\frac{\partial v}{\partial T}\right)_p^2 \tag{A4}$$

The ratio of the two work expressions is

$$\frac{di}{di^*} = -\frac{\dfrac{\gamma}{(\gamma-1)}\,T\left(\dfrac{\partial v}{\partial T}\right)_T\left(\dfrac{\partial v}{\partial T}\right)_p^2}{\dfrac{ZR\gamma}{(\gamma-1)}} - \frac{\left[T\left(\dfrac{\partial v}{\partial T}\right)_p - v\right] dp}{\dfrac{ZR\gamma}{(\gamma-1)}\,dT} \tag{A5}$$

or $di/di^* = -A - B$, where the first term is

$$A = T\left(\frac{\partial p}{\partial v}\right)_T\left(\frac{\partial v}{\partial T}\right)_p^2 / ZR \tag{A6}$$

Expanding A gives

$$A = -1 + \left[v\left(\frac{\partial Z}{\partial v}\right)_T/Z\right] - \left[2T\left(\frac{\partial Z}{\partial T}\right)_p/Z\right] + \left[2vT\left(\frac{\partial Z}{\partial T}\right)_p\left(\frac{\partial Z}{\partial v}\right)_T/Z^2\right] - \left[T^2\left(\frac{\partial Z}{\partial T}\right)_p^2/Z^2\right] + T^2\left(v\frac{\partial Z}{\partial T}\right)_p^2\left(\frac{\partial Z}{\partial v}\right)_T/Z^3 \tag{A7}$$

The second term is given by

$$B = (\gamma-1)\left[T\left(\frac{\partial v}{\partial T}\right)_p - v\right] dp/ZR\gamma dT \tag{A8}$$

Assuming an isentropic process,

$$\frac{dp}{dT} = -\frac{\gamma}{(\gamma-1)}\left(\frac{\partial p}{\partial v}\right)_T\left(\frac{\partial v}{\partial T}\right)_p \tag{A9}$$

For a real process, $dT_{real} = \eta dT_{ideal}$, but $dp_{real} = dp_{ideal}$. Then B becomes

$$B = -Tv\left(\frac{\partial Z}{\partial T}\right)_p/\eta Z^2R\left(\frac{\partial p}{\partial v}\right)_T\left(\frac{\partial v}{\partial T}\right)_p \tag{A10}$$

$$B = -Tv\left[\left(\frac{\partial Z}{\partial T}\right)_p/\eta Z^2R\right]\left[-\frac{ZRT}{v^2} + \frac{RT(\partial Z/\partial v)_T}{v}\right] \times \left[\frac{ZR}{p} + RT\left(\frac{\partial Z}{\partial T}\right)_p/p\right] \tag{A11}$$

Retaining only the first-order derivatives of Z gives

$$\frac{di}{di^*} \approx 1 - \left[v\left(\frac{\partial Z}{\partial v}\right)_T/Z\right] + \left[(2\eta-1)T\left(\frac{\partial z}{\partial T}\right)_p/\eta Z\right] \tag{A12}$$

The two partials can be evaluated from the gas properties. For the baseline inlet conditions $[v(\partial Z/\partial v)_T]/Z = -0.069$ and $[T(\partial Z/\partial T)_v]/Z = -0.058$. The value of η is ≈ 0.9, so that the correction is less than 2%.

Appendix B: Coordinates for Alternate Designs

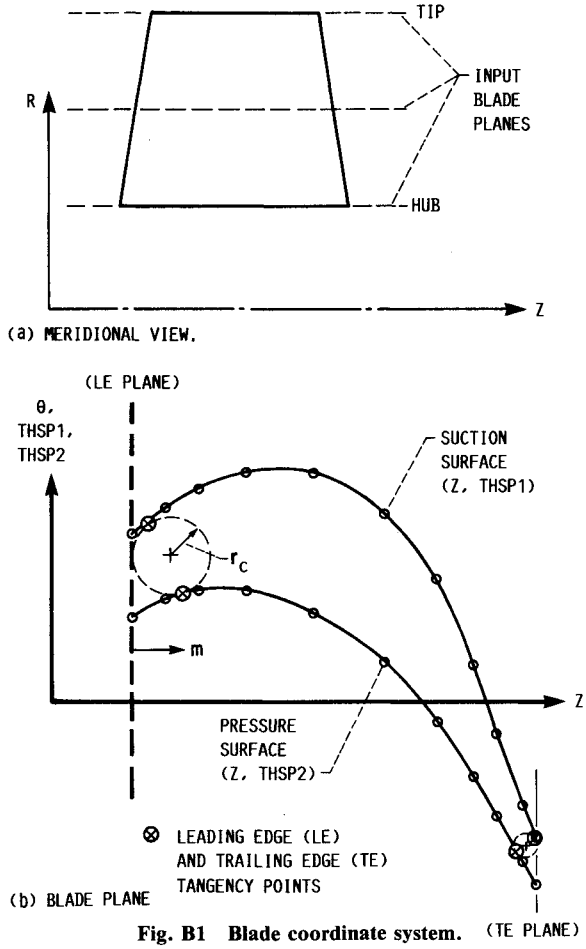

Fig. B1 Blade coordinate system.

Table B1 Blade coordinates for revised first-stage rotor

	R 11.82013			R 12.94180			R 14.06346		
	Z	THSP1	THSP2	Z	THSP1	THSP2	Z	THSP1	THSP2
1	-0.95874	-0.00537	-0.03683	-0.80969	0.02096	-0.00686	-0.66065	0.04729	0.02311
2	-0.89786	0.00659	-0.03464	-0.75477	0.02884	-0.00517	-0.61168	0.05108	0.02430
3	-0.83697	0.01767	-0.03258	-0.69984	0.03617	-0.00359	-0.56271	0.05466	0.02540
4	-0.77609	0.02773	-0.03067	-0.64492	0.04286	-0.00214	-0.51375	0.05798	0.02639
5	-0.71521	0.03662	-0.02892	-0.59000	0.04882	-0.00083	-0.46478	0.06101	0.02727
6	-0.65433	0.04419	-0.02735	-0.53507	0.05395	0.00032	-0.41581	0.06372	0.02800
7	-0.59345	0.05035	-0.02599	-0.48015	0.05820	0.00130	-0.36685	0.06606	0.02859
8	-0.53257	0.05519	-0.02478	-0.42522	0.06161	0.00211	-0.31788	0.06802	0.02901
9	-0.47168	0.05890	-0.02370	-0.37030	0.06425	0.00278	-0.26891	0.06960	0.02925
10	-0.41080	0.06166	-0.02268	-0.31537	0.06621	0.00332	-0.21994	0.07077	0.02931
11	-0.34992	0.06365	-0.02168	-0.26045	0.06758	0.00374	-0.17098	0.07151	0.02917
12	-0.28904	0.06503	-0.02067	-0.20552	0.06843	0.00407	-0.12201	0.07182	0.02880
13	-0.22816	0.06589	-0.01970	-0.15060	0.06879	0.00423	-0.07304	0.07169	0.02816
14	-0.16728	0.06629	-0.01883	-0.09568	0.06870	0.00420	-0.02408	0.07111	0.02722
15	-0.10639	0.06633	-0.01812	-0.04075	0.06820	0.00390	0.02489	0.07007	0.02592
16	-0.04551	0.06607	-0.01762	0.01417	0.06732	0.00330	0.07386	0.06856	0.02423
17	0.01537	0.06550	-0.01738	0.06910	0.06604	0.00238	0.12282	0.06658	0.02213
18	0.07625	0.06451	-0.01740	0.12402	0.06430	0.00114	0.17179	0.06409	0.01969
19	0.13713	0.06297	-0.01769	0.17894	0.06201	-0.00037	0.22076	0.06106	0.01695
20	0.19801	0.06077	-0.01826	0.23387	0.05911	-0.00214	0.26973	0.05746	0.01398
21	0.25890	0.05779	-0.01912	0.28879	0.05552	-0.00414	0.31869	0.05326	0.01084
22	0.31978	0.05392	-0.02028	0.34372	0.05117	-0.00638	0.36766	0.04842	0.00753
23	0.38066	0.04906	-0.02174	0.39864	0.04598	-0.00886	0.41663	0.04290	0.00401
24	0.44154	0.04309	-0.02350	0.45357	0.03988	-0.01162	0.46559	0.03667	0.00025
25	0.50242	0.03590	-0.02556	0.50849	0.03280	-0.01468	0.51456	0.02969	-0.00381
26	0.56330	0.02746	-0.02794	0.56341	0.02468	-0.01807	0.56353	0.02191	-0.00820
27	0.62418	0.01792	-0.03076	0.61834	0.01568	-0.02187	0.61249	0.01343	-0.01298
28	0.68507	0.00754	-0.03419	0.67326	0.00599	-0.02618	0.66146	0.00444	-0.01818
29	0.74595	-0.00345	-0.03837	0.72819	-0.00416	-0.03111	0.71043	-0.00487	-0.02385
30	0.80683	-0.01481	-0.04347	0.78311	-0.01457	-0.03675	0.75939	-0.01433	-0.03004
31	0.86771	-0.02637	-0.04954	0.83804	-0.02505	-0.04317	0.80836	-0.02374	-0.03680
32	0.92859	-0.03811	-0.05653	0.89296	-0.03558	-0.05031	0.85733	-0.03305	-0.04410
33	0.98948	-0.05000	-0.06431	0.94789	-0.04614	-0.05809	0.90630	-0.04227	-0.05188
34	1.05035	-0.06203	-0.07281	1.00281	-0.05672	-0.06644	0.95526	-0.05142	-0.06007
35	1.11123	-0.07417	-0.08191	1.05773	-0.06734	-0.07527	1.00423	-0.06051	-0.06862
	LEADING EDGE		TRAILING EDGE	LEADING EDGE		TRAILING EDGE	LEADING EDGE		TRAILING EDGE
r_c	0.22684		0.02270	0.21925		0.02230	0.19871		0.02151
R	11.82013		11.82013	12.94180		12.94180	14.06346		14.06345
z_0	-0.73190		1.08853	-0.59044		1.03543	-0.46194		0.98272
m_0	0.22684		2.04727	0.21925		1.84512	0.19871		1.64336
θ_0	-0.00926		-0.07456	0.01673		-0.06767	0.04177		-0.06079
m_{t1}	0.01808		2.06818	0.02610		1.86583	0.05455		1.66344
θ_{t1}	-0.00175		-0.07381	0.02476		-0.06703	0.05150		-0.06024
m_{t2}	0.29069		2.02756	0.27283		1.82507	0.23715		1.62347
θ_{t2}	-0.02769		-0.07551	0.00029		-0.06842	0.02790		-0.06137

Z - Axial coordinate of blade surfaces, (cm)
R - Radial distance from centerline, (cm)
THSP1 - Tangential coordinate of blade surface 1, (rad)
THSP2 - Tangential coordinate of blade surface 2, (rad)
r_c - Radius of leading or trailing edge circle, (cm)
m_0 - Meridional coordinate of center of leading or trailing edge circle, (cm)
z_0 - Axial coordinate of center of leading or trailing edge circle, (cm)
θ_0 - Tangential coordinate of center of leading or trailing edge circle, (rad)
m_{t1} - Meridional coordinate of tangency point on surface 1, (cm)
θ_{t1} - Tangential coordinate of tangency point on surface 1, (rad)
m_{t2} - Meridional coordinate of tangency point on surface 2, (cm)
θ_{t2} - Tangential coordinate of tangency point on surface 2, (rad)

Table B2 Blade coordinates for stator of single-stage design

	R 11.43000			R 12.81074			R 14.19148		
	Z	THSP1	THSP2	Z	THSP1	THSP2	Z	THSP1	THSP2
1	0.00000	0.32500	0.23500	0.00000	0.27775	0.21150	0.00000	0.23050	0.18800
2	0.07593	0.32780	0.23175	0.07763	0.28041	0.20869	0.07934	0.23301	0.18562
3	0.15186	0.33025	0.22840	0.15527	0.28276	0.20583	0.15868	0.23527	0.18326
4	0.22779	0.33229	0.22492	0.23290	0.28476	0.20292	0.23801	0.23723	0.18092
5	0.30372	0.33386	0.22131	0.31054	0.28635	0.19996	0.31735	0.23885	0.17861
6	0.37966	0.33490	0.21753	0.38817	0.28749	0.19692	0.39669	0.24009	0.17631
7	0.45559	0.33536	0.21360	0.46581	0.28814	0.19381	0.47603	0.24091	0.17403
8	0.53152	0.33522	0.20954	0.54344	0.28826	0.19062	0.55536	0.24130	0.17169
9	0.60745	0.33443	0.20542	0.62107	0.28784	0.18732	0.63470	0.24126	0.16923
10	0.68338	0.33297	0.20131	0.69871	0.28688	0.18393	0.71404	0.24078	0.16656
11	0.75931	0.33083	0.19726	0.77634	0.28534	0.18043	0.79337	0.23986	0.16361
12	0.83524	0.32797	0.19332	0.85398	0.28323	0.17683	0.87271	0.23848	0.16034
13	0.91117	0.32443	0.18939	0.93161	0.28053	0.17307	0.95205	0.23664	0.15676
14	0.98710	0.32029	0.18525	1.00924	0.27729	0.16909	1.03139	0.23429	0.15293
15	1.06303	0.31562	0.18069	1.08688	0.27353	0.16478	1.11072	0.23144	0.14887
16	1.13896	0.31050	0.17552	1.16451	0.26927	0.16007	1.19006	0.22805	0.14462
17	1.21490	0.30495	0.16956	1.24215	0.26449	0.15488	1.26940	0.22403	0.14019
18	1.29083	0.29881	0.16286	1.31978	0.25902	0.14921	1.34874	0.21923	0.13555
19	1.36676	0.29185	0.15555	1.39742	0.25268	0.14311	1.42807	0.21350	0.13066
20	1.44269	0.28382	0.14775	1.47505	0.24526	0.13663	1.50741	0.20670	0.12550
21	1.51862	0.27450	0.13959	1.55268	0.23660	0.12979	1.58675	0.19869	0.12000
22	1.59455	0.26369	0.13109	1.63032	0.22658	0.12249	1.66609	0.18948	0.11390
23	1.67048	0.25128	0.12195	1.70795	0.21520	0.11442	1.74543	0.17912	0.10689
24	1.74641	0.23723	0.11181	1.78559	0.20245	0.10523	1.82476	0.16767	0.09865
25	1.82234	0.22146	0.10029	1.86322	0.18831	0.09458	1.90410	0.15516	0.08887
26	1.89827	0.20390	0.08703	1.94085	0.17275	0.08214	1.98343	0.14160	0.07726
27	1.97420	0.18447	0.07170	2.01848	0.15559	0.06778	2.06277	0.12670	0.06386
28	2.05013	0.16291	0.05434	2.09612	0.13649	0.05156	2.14211	0.11008	0.04878
29	2.12606	0.13886	0.03515	2.17375	0.11511	0.03365	2.22144	0.09135	0.03215
30	2.20199	0.11198	0.01433	2.25139	0.09105	0.01422	2.30078	0.07013	0.01411
31	2.27793	0.08192	-0.00792	2.32902	0.06402	-0.00658	2.38012	0.04613	-0.00524
32	2.35386	0.04838	-0.03139	2.40665	0.03395	-0.02857	2.45946	0.01952	-0.02575
33	2.42979	0.01156	-0.05592	2.48429	0.00108	-0.05161	2.53879	-0.00939	-0.04730
34	2.50572	-0.02807	-0.08134	2.56192	-0.03420	-0.07555	2.61813	-0.04033	-0.06976
35	2.58165	-0.07000	-0.10750	2.63956	-0.07150	-0.10025	2.69747	-0.07300	-0.09300
	LEADING EDGE		TRAILING EDGE	LEADING EDGE		TRAILING EDGE	LEADING EDGE		TRAILING EDGE
r_c	0.65933		0.05332	0.59725		0.04417	0.44406		0.03325
R	11.42999		11.42999	12.81073		12.81073	14.19148		14.19147
z_0	0.65933		2.52833	0.59725		2.59538	0.44406		2.66422
m_0	0.65933		2.52833	0.59725		2.59538	0.44406		2.66420
θ_0	0.26998		-0.07036	0.24092		-0.07177	0.20880		-0.07319
m_{t1}	1.04628		2.58102	0.74222		2.63900	0.34239		2.69699
θ_{t1}	0.31670		-0.06964	0.28609		-0.07123	0.23928		-0.07281
m_{t2}	0.33486		2.47673	0.33118		2.55253	0.27386		2.63188
θ_{t2}	0.21978		-0.07153	0.19916		-0.07261	0.17987		-0.07375

Table B3 Blade coordinates for rotor of single-stage design

	R 11.43000			R 12.81074			R 14.19148		
	Z	THSP1	THSP2	Z	THSP1	THSP2	Z	THSP1	THSP2
1	-0.97536	0.11000	0.01900	-0.82296	0.10600	0.06000	-0.67056	0.11500	0.06800
2	-0.85703	0.14896	0.03457	-0.70911	0.12471	0.06373	-0.56119	0.12843	0.07339
3	-0.73869	0.17846	0.04721	-0.59526	0.14219	0.06770	-0.45182	0.14225	0.07857
4	-0.62036	0.20028	0.05720	-0.48141	0.15792	0.07168	-0.34245	0.15567	0.08343
5	-0.50202	0.21743	0.06515	-0.36755	0.17152	0.07537	-0.23308	0.16766	0.08784
6	-0.38369	0.23093	0.07134	-0.25370	0.18297	0.07867	-0.12372	0.17788	0.09176
7	-0.26536	0.24115	0.07592	-0.13985	0.19247	0.08158	-0.01435	0.18646	0.09518
8	-0.14702	0.24848	0.07906	-0.02600	0.20020	0.08410	0.09502	0.19353	0.09811
9	-0.02869	0.25328	0.08092	0.08785	0.20636	0.08625	0.20439	0.19923	0.10055
10	0.08965	0.25593	0.08166	0.20170	0.21113	0.08803	0.31376	0.20369	0.10248
11	0.20798	0.25681	0.08144	0.31555	0.21470	0.08944	0.42313	0.20705	0.10391
12	0.32631	0.25628	0.08041	0.42941	0.21727	0.09049	0.53250	0.20943	0.10484
13	0.44465	0.25474	0.07874	0.54326	0.21902	0.09119	0.64187	0.21098	0.10526
14	0.56298	0.25253	0.07657	0.65711	0.22013	0.09153	0.75124	0.21183	0.10517
15	0.68131	0.24973	0.07398	0.77096	0.22072	0.09150	0.86061	0.21211	0.10457
16	0.79965	0.24624	0.07095	0.88481	0.22064	0.09104	0.96998	0.21180	0.10345
17	0.91798	0.24195	0.06747	0.99867	0.21972	0.09007	1.07935	0.21082	0.10179
18	1.03632	0.23674	0.06353	1.11252	0.21779	0.08852	1.18871	0.20906	0.09960
19	1.15465	0.23051	0.05913	1.22637	0.21467	0.08630	1.29809	0.20643	0.09685
20	1.27298	0.22314	0.05426	1.34022	0.21020	0.08335	1.40745	0.20283	0.09352
21	1.39132	0.21453	0.04891	1.45407	0.20420	0.07958	1.51682	0.19815	0.08962
22	1.50965	0.20456	0.04307	1.56792	0.19650	0.07493	1.62619	0.19230	0.08513
23	1.62799	0.19313	0.03674	1.68177	0.18692	0.06932	1.73556	0.18518	0.08002
24	1.74632	0.18011	0.02989	1.79562	0.17530	0.06267	1.84492	0.17669	0.07430
25	1.86465	0.16537	0.02240	1.90947	0.16151	0.05492	1.95430	0.16674	0.06795
26	1.98299	0.14871	0.01405	2.02332	0.14566	0.04604	2.06366	0.15523	0.06094
27	2.10132	0.12998	0.00462	2.13717	0.12791	0.03603	2.17303	0.14211	0.05320
28	2.21966	0.10898	-0.00610	2.25102	0.10843	0.02487	2.28240	0.12734	0.04467
29	2.33799	0.08555	-0.01835	2.36487	0.08736	0.01257	2.39177	0.11086	0.03529
30	2.45632	0.05961	-0.03224	2.47872	0.06489	-0.00090	2.50114	0.09262	0.02498
31	2.57466	0.03132	-0.04767	2.59257	0.04115	-0.01550	2.61051	0.07257	0.01369
32	2.69299	0.00091	-0.06449	2.70642	0.01627	-0.03111	2.71988	0.05078	0.00144
33	2.81133	-0.03142	-0.08258	2.82027	-0.00963	-0.04764	2.82924	0.02746	-0.01167
34	2.92966	-0.06546	-0.10180	2.93412	-0.03642	-0.06497	2.93861	0.00279	-0.02552
35	3.04800	-0.10100	-0.12200	3.04797	-0.06399	-0.08300	3.04798	-0.02300	-0.04000
	LEADING EDGE		TRAILING EDGE	LEADING EDGE		TRAILING EDGE	LEADING EDGE		TRAILING EDGE
r_c	0.42413		0.05590	0.33800		0.05469	0.31950		0.05812
R	11.42999		11.42999	12.81074		12.81073	14.19148		14.19147
z_0	-0.55123		2.99209	-0.48496		2.99328	-0.35106		2.98986
m_0	0.42413		3.96746	0.33800		3.81625	0.31950		3.66041
θ_0	0.10552		-0.10169	0.10014		-0.06466	0.10894		-0.02359
m_{t1}	0.01233		4.02119	0.03203		3.86834	0.04270		3.71617
θ_{t1}	0.11441		-0.10034	0.11136		-0.06336	0.12019		-0.02243
m_{t2}	0.61145		3.91788	0.46109		3.76733	0.46761		3.60933
θ_{t2}	0.07221		-0.10395	0.07554		-0.06657	0.08897		-0.02554

Table B4 Blade coordinates for exit guide vane of single-stage design

	Z	R	THSP1	THSP2	Z	R	THSP1	THSP2	Z	R	THSP1	THSP2
1	0.00000	11.43000	0.05540	0.04900	0.26642	12.13933	0.11929	0.11224	0.55790	12.83820	0.17085	0.16378
2	0.21515	11.43000	0.12002	0.06711	0.47306	12.13756	0.16598	0.12891	0.75536	12.83520	0.20451	0.17827
3	0.43030	11.42999	0.18121	0.09142	0.67954	12.13524	0.20569	0.14816	0.95244	12.83112	0.23002	0.19316
4	0.64546	11.42999	0.23890	0.11828	0.88587	12.13235	0.24003	0.16865	1.14918	12.82591	0.25031	0.20848
5	0.86061	11.42999	0.28901	0.14371	1.09208	12.12894	0.26973	0.18794	1.34564	12.81963	0.26777	0.22302
6	1.07576	11.43000	0.33158	0.16730	1.29821	12.12504	0.29566	0.20573	1.54190	12.81238	0.28325	0.23651
7	1.29092	11.43000	0.36730	0.18919	1.50428	12.12069	0.31818	0.22215	1.73803	12.80423	0.29697	0.24908
8	1.50607	11.43000	0.39685	0.20951	1.71033	12.11593	0.33761	0.23737	1.93408	12.79526	0.30918	0.26080
9	1.72122	11.43000	0.42093	0.22842	1.91637	12.11081	0.35429	0.25153	2.13012	12.78553	0.32009	0.27178
10	1.93637	11.43000	0.44023	0.24605	2.12244	12.10535	0.36854	0.26479	2.32620	12.77512	0.32991	0.28211
11	2.15152	11.43000	0.45544	0.26253	2.32857	12.09963	0.38067	0.27729	2.52238	12.76416	0.33885	0.29190
12	2.36667	11.43000	0.46724	0.27801	2.53478	12.09375	0.39101	0.28917	2.71875	12.75287	0.34710	0.30125
13	2.58182	11.42999	0.47633	0.29263	2.74113	12.08783	0.39996	0.30056	2.91539	12.74148	0.35489	0.31026
14	2.79698	11.42999	0.48340	0.30652	2.94763	12.08201	0.40795	0.31156	3.11236	12.73025	0.36246	0.31902
15	3.01213	11.43000	0.48913	0.31983	3.15432	12.07640	0.41531	0.32223	3.30974	12.71942	0.36989	0.32756
16	3.22728	11.43000	0.49415	0.33268	3.36121	12.07114	0.42227	0.33264	3.50755	12.70926	0.37720	0.33588
17	3.44243	11.43000	0.49867	0.34513	3.56833	12.06635	0.42891	0.34277	3.70584	12.70002	0.38434	0.34399
18	3.65759	11.43000	0.50273	0.35719	3.77566	12.06212	0.43520	0.35265	3.90460	12.69187	0.39128	0.35188
19	3.87274	11.43000	0.50636	0.36888	3.98319	12.05842	0.44115	0.36224	4.10378	12.68475	0.39799	0.35953
20	4.08789	11.42999	0.50961	0.38023	4.19089	12.05522	0.44674	0.37156	4.30333	12.67862	0.40443	0.36694
21	4.30304	11.43000	0.51250	0.39125	4.39874	12.05249	0.45200	0.38060	4.50319	12.67340	0.41059	0.37408
22	4.51820	11.43000	0.51508	0.40196	4.60671	12.05020	0.45691	0.38936	4.70333	12.66904	0.41644	0.38096
23	4.73335	11.43000	0.51739	0.41238	4.81479	12.04831	0.46147	0.39782	4.90370	12.66546	0.42195	0.38755
24	4.94850	11.43000	0.51946	0.42254	5.02297	12.04678	0.46570	0.40601	5.10426	12.66259	0.42710	0.39386
25	5.16365	11.43000	0.52133	0.43245	5.23121	12.04558	0.46959	0.41390	5.30497	12.66035	0.43188	0.39987
26	5.37880	11.43000	0.52303	0.44213	5.43951	12.04466	0.47315	0.42150	5.50580	12.65867	0.43626	0.40557
27	5.59395	11.43000	0.52461	0.45160	5.64786	12.04401	0.47636	0.42882	5.70672	12.65750	0.44021	0.41096
28	5.80911	11.43000	0.52609	0.46088	5.85624	12.04357	0.47925	0.43584	5.90771	12.65675	0.44372	0.41603
29	6.02426	11.43000	0.52753	0.47000	6.06464	12.04333	0.48180	0.44258	6.10875	12.65638	0.44676	0.42078
30	6.23941	11.42999	0.52894	0.47896	6.27306	12.04325	0.48403	0.44905	6.30981	12.65631	0.44932	0.42521
31	6.45456	11.43000	0.53036	0.48779	6.48148	12.04330	0.48596	0.45525	6.51089	12.65648	0.45146	0.42934
32	6.66972	11.43000	0.53177	0.49649	6.68991	12.04345	0.48763	0.46123	6.71198	12.65684	0.45320	0.43320
33	6.88487	11.42999	0.53318	0.50509	6.89833	12.04366	0.48907	0.46700	6.91305	12.65730	0.45459	0.43683
34	7.10002	11.43000	0.53459	0.51358	7.10675	12.04391	0.49029	0.47258	7.11412	12.65783	0.45566	0.44023
35	7.31517	11.43000	0.53600	0.52200	7.31517	12.04416	0.49133	0.47800	7.31517	12.65833	0.45646	0.44345

	LEADING EDGE	TRAILING EDGE	LEADING EDGE	TRAILING EDGE	LEADING EDGE	TRAILING EDGE
r_c	0.03172	0.09258	0.03465	0.08934	0.03624	0.08809
R	11.42999	11.42999	12.13908	12.04406	12.83776	12.65812
z_0	0.03172	7.22259	0.30107	7.22582	0.59413	7.22708
m_0	0.03172	7.22259	0.03465	6.96041	0.03624	6.67306
θ_0	0.05501	0.52726	0.11881	0.48347	0.17029	0.44917
m_{t1}	0.00122	7.21569	0.00189	6.95509	0.00280	6.66869
θ_{t1}	0.05577	0.53535	0.11974	0.49088	0.17138	0.45612
m_{t2}	0.05269	7.26031	0.05049	6.98699	0.06104	6.69044
θ_{t2}	0.05293	0.51986	0.11674	0.47638	0.16823	0.44234

	Z	R	THSP1	THSP2	Z	R	THSP1	THSP2
1	0.87881	13.52401	0.20703	0.20068	1.22304	14.19879	0.23020	0.22522
2	1.06642	13.52046	0.23378	0.21206	1.40040	14.19522	0.25519	0.23268
3	1.25339	13.51529	0.25416	0.22345	1.57682	14.18952	0.27815	0.24127
4	1.43975	13.50843	0.27204	0.23512	1.75233	14.18156	0.30352	0.25051
5	1.62562	13.49998	0.28754	0.24660	1.92710	14.17149	0.32588	0.26035
6	1.81113	13.49006	0.30033	0.25771	2.10131	14.15944	0.34279	0.27066
7	1.99638	13.47878	0.31085	0.26841	2.27510	14.14556	0.35506	0.28118
8	2.18147	13.46625	0.31951	0.27866	2.44864	14.13000	0.36360	0.29166
9	2.36651	13.45257	0.32676	0.28841	2.62203	14.11288	0.36930	0.30187
10	2.55157	13.43784	0.33302	0.29764	2.79542	14.09432	0.37303	0.31159
11	2.73676	13.42224	0.33868	0.30634	2.96894	14.07459	0.37563	0.32062
12	2.92225	13.40612	0.34409	0.31451	3.14283	14.05411	0.37786	0.32882
13	3.10814	13.38982	0.34946	0.32222	3.31725	14.03334	0.38002	0.33622
14	3.29457	13.37370	0.35494	0.32956	3.49239	14.01278	0.38219	0.34293
15	3.48162	13.35815	0.36052	0.33659	3.66838	13.99291	0.38443	0.34904
16	3.66937	13.34354	0.36615	0.34331	3.84533	13.97425	0.38677	0.35462
17	3.85789	13.33028	0.37178	0.34974	4.02333	13.95733	0.38922	0.35974
18	4.04716	13.31859	0.37737	0.35591	4.20238	13.94246	0.39176	0.36446
19	4.23711	13.30842	0.38287	0.36181	4.38236	13.92956	0.39436	0.36882
20	4.42765	13.29969	0.38825	0.36744	4.56316	13.91853	0.39698	0.37284
21	4.61870	13.29229	0.39347	0.37281	4.74467	13.90925	0.39960	0.37656
22	4.81018	13.28614	0.39849	0.37791	4.92677	13.90157	0.40218	0.37999
23	5.00204	13.28113	0.40328	0.38274	5.10937	13.89538	0.40468	0.38317
24	5.19418	13.27715	0.40780	0.38730	5.29238	13.89052	0.40709	0.38612
25	5.38657	13.27410	0.41201	0.39159	5.47572	13.88686	0.40939	0.38887
26	5.57915	13.27186	0.41590	0.39561	5.65931	13.88423	0.41154	0.39144
27	5.77187	13.27033	0.41943	0.39937	5.84309	13.88253	0.41354	0.39385
28	5.96469	13.26943	0.42257	0.40287	6.02700	13.88162	0.41537	0.39615
29	6.15759	13.26905	0.42531	0.40611	6.21100	13.88137	0.41703	0.39835
30	6.35052	13.26911	0.42762	0.40910	6.39505	13.88166	0.41851	0.40047
31	6.54347	13.26950	0.42955	0.41185	6.57912	13.88235	0.41982	0.40252
32	6.73642	13.27013	0.43111	0.41439	6.76317	13.88333	0.42098	0.40449
33	6.92936	13.27090	0.43236	0.41674	6.94720	13.88446	0.42200	0.40640
34	7.12227	13.27173	0.43333	0.41891	7.13120	13.88562	0.42290	0.40826
35	7.31517	13.27250	0.43406	0.42094	7.31517	13.88668	0.42369	0.41007

	LEADING EDGE	TRAILING EDGE	LEADING EDGE	TRAILING EDGE
r_c	0.03670	0.09057	0.03637	0.09779
R	13.52348	13.27216	14.19829	13.88614
z_0	0.91551	7.22460	1.25940	7.21737
m_0	0.03670	6.35399	0.03637	6.00813
θ_0	0.20642	0.42690	0.22962	0.41622
m_{t1}	0.00351	6.34953	0.00353	6.00226
θ_{t1}	0.20758	0.43372	0.23072	0.42326
m_{t2}	0.05999	6.36644	0.05459	6.02137
θ_{t2}	0.20432	0.42014	0.22740	0.40924

References

[1]Moffitt, T. P., Szanca, E. M., Whitney, W. J., and Behning, F. P., "Design and Cold-Air Test of Single-Stage Uncooled Core Turbine with High Work Output," NASA TP-1680, June 1980.

[2]Thulin, R. D., Howe, D. C., and Singer, I. D., "Energy Efficient Engine High-Pressure Turbine Detailed Design Report," Pratt and Whitney Aircraft Group, East Hartford, CT, PWA-5594-171, NASA CR-165608, Jan. 1982.

[3]Engineering Staff, "Low-Aspect-Ratio Turbine Technology Program," Airesearch Manufacturing Co., Pheonix, AZ, Rept. 75-211701(2), 1977.

[4]Katsanis, T., and McNally, W. D., "Revised Fortran Program for Calculating Velocities and Streamlines on the Hub-Shroud Midchannel Stream Surface of an Axial-, Radial-, or Mixed-Flow Turbomachine or Annular Duct, Vol. I—User's Manual," NASA TN D-8430, March 1977.

[5]McFarland, E. R., "A Rapid Blade-to-Blade Solution for Use in Turbomachinery Design," *Journal of Engineering for Gas Turbines and Power,* Vol. 106, No. 2, April 1984, pp. 376-382.

[6]Boyle, R. J., Haas, J. E., and Katsanis, T., "Comparison Between Measured Turbine Stage Performance and the Predicted Performance Using Quasi-Three-Dimensional Flow and Boundary-Layer Analyses," AIAA Paper 84-1299, June 1984.

[7]Crawford, M. E., and Kays, W. M., "STAN5—A Program for Numerical Computation of Two-Dimensional Internal and External Boundary Layer Flows," NASA CR-2742, Dec. 1976.

[8]McNally, W. D., "Fortran Program for Calculating Compressible Laminar and Turbulent Boundary Layers in Arbitrary Pressure Gradients," NASA TN D-5681, May 1970.

[9]Hendricks, R. C., Peller, I. C., and Baron, A. K., "WASP—A Flexible Fortran IV Computer Code for Calculating Water and Stream Properties," NASA TN D-7391, Nov. 1973.

[10]Hendricks, R. C., Baron, A. K., and Peller, I. C., "GASP—A Computer Code for Calculating the Thermodynamic and Transport Properties for Ten Fluids: Parahydrogen, Helium, Neon, Methane, Nitrogen, Carbon Monoxide, Fluorine, Argon, and Carbon Dioxide," NASA TN D-7808, Feb. 1975.

[11]Žukauskas, A., and Žiugžda, J., *Heat Transfer of a Cylinder in Crossflow,* Hemisphere, Washington, DC, 1985, Chap. 6, p. 112, and Appendix, p. 168.

[12]Lowery, G. W., and Vachon, R. I., "The Effect of Turbulence on Heat Transfer from Heated Cylinders," *International Journal of Heat and Mass Transfer,* Vol. 18, No. 11, Nov. 1975, pp. 1229-1242.

[13]O'Brien, J. E., and Van Fossen, G. J., "The Influence of Jet-Grid Turbulence on Heat Transfer from the Stagnation Region of a Cylinder in Crossflow," American Society of Mechanical Engineers, New York, ASME Paper 85-HT-58, Aug. 1985.

[14]Schwab, J. R., "Aerodynamic Performance of High Turning Core Turbine Vanes in a Two-Dimensional Cascade," AIAA Paper 82-1288, June 1982.

[15]Ewen, J. S., Huber, F. W., and Mitchell, J. P., "Investigation of the Aerodynamic Performance of Small Axial Turbines," American Society of Mechanical Engineers, New York, ASME Paper 73-GT-3, April 1973.

[16]Sanz, J. M., "Automated Design of Controlled Diffusion Blades," *Journal of Turbomachinery,* Vol. 110, No. 4, Oct. 1988, pp. 540-544.